Word count: 6604

Revision 1

Synthesis of calcium orthocarbonate, Ca_2CO_4-*Pnma* at *p, T*-conditions of Earth's transition zone and lower mantle

Jannes Binck[1,]*, Dominique Laniel[2], Lkhamsuren Bayarjargal[1], Saiana Khandarkhaeva[3], Timofey Fedotenko[2], Andrey Aslandukov[2], Konstantin Glazyrin[4], Victor Milman[5], Stella Chariton[6], Vitali B. Prakapenka[6], Natalia Dubrovinskaia[2], Leonid Dubrovinsky[3], Björn Winkler[1]

[1]Institut für Geowissenschaften, Goethe-Universität Frankfurt, Altenhöferallee 1, 60438 Frankfurt am Main, Germany

[2]Laboratory of Crystallography, University of Bayreuth, 95440 Bayreuth, Germany

[3]Bayerisches Geoinstitut, University of Bayreuth, 95440, Bayreuth, Germany

[4]Photon Science, Deutsches Elektronen-Synchrotron, Notkestrasse 85, 22607, Hamburg, Germany

[5]BIOVIA Dassault Systèmes, 334 Science Park, Cambridge CB4 0WN, UK

[6]Center for Advanced Radiation Sources, University of Chicago, Chicago, Illinois 60637, United States.

*Correspondence to: J. Binck (binck@kristall.uni-frankfurt.de)

Abstract

We show, by single crystal diffraction studies in laser-heated diamond anvil cells, that Ca_2CO_4 orthocarbonate, which contains CO_4^{4-} tetrahedra, can be formed already at ~20 GPa at ~1830 K, i.e. at much lower pressures than other carbonates with *sp*^{3}-hybridized carbon. Ca_2CO_4 can also be formed at ~89 GPa and ~2500 K. This very broad *p, T*-range suggests the possible existence of Ca_2CO_4 in the Earth's transition zone and in most of the lower mantle. Raman spectroscopy shows the typical bands associated with tetrahedral CO_4^{4-}-groups. DFT-theory based calculations reproduce the experimental Raman spectra and indicate that at least in the athermal limit the phase assemblage of $Ca_2CO_4 + 2SiO_2$ is more stable than $2CaSiO_3 + CO_2$ at high pressures.

Keywords: carbonate, Ca_2CO_4, structure, x-ray diffraction, Raman spectroscopy, density functional theory

Introduction

Carbonates play a crucial role in the long-term global carbon cycle as they contain ≈ 60 - 70% of the carbon present on Earth's surface and in its crust (Hirschmann, 2010; McKenzie et al., 2016; Ridgwell, 2005; Wallmann, 2001). As carbonates are partly incorporated into oceanic lithosphere, they may be transported into the deep mantle via subduction (Clift, 2017; Kelemen and Manning 2015; McKenzie et al., 2016). Models propose a carbon influx on the order of several tenth-megatons per year, which is mainly due to the contribution of carbonate sediments and altered carbonaceous oceanic crust (Hirschmann, 2010; Kelemen and Manning, 2015). Within the last two decades, several studies showed that all major carbonates, such as $CaCO_3$ (Bayarjargal et al., 2018), $MgCO_3$ (Binck et al., 2020b), $FeCO_3$ (Cerantola et al., 2017) and

$CaMg(CO_3)_2$ (Binck et al., 2020a; Merlini et al., 2017), may be stable at the *p, T* conditions of the Earth's mantle, while displaying a variety of different high *p, T* structures (e.g. Binck et al., 2020a; Cerantola et al., 2017; Chariton et al., 2020; Merlini et al., 2017; Gavryushkin et al., 2017; Ono et al., 2007). It has been proposed that carbonates in contact with mantle silicates and metals in the deep Earth are reduced and, depending on the stage of reduction, form metal carbides, or diamonds (Palyanov et al., 2013; Rohrbach et al., 2011; Stagno et al., 2012, 2013). However, carbonate inclusions in diamonds originating from the deep mantle offer direct evidence for the presence of oxidized carbon in the form of carbonates in at least some regions of the mantle (Brenker et al., 2007; Kaminsky et al., 2016). Cold oxidized subducting slabs with low reaction kinetics are believed to provide suitable conditions for hosting carbonates even at depths of the lower mantle (Maeda et al., 2017; Martirosyan et al., 2016; Walter et al., 2011).

A recent remarkable discovery are carbonates, in which sp^3-hybridization of carbon leads to the formation of CO_4^{4-} tetrahedra instead of triangular sp^2-hybridized CO_3^{3-}-groups (Binck et al., 2020b; Boulard et al., 2011, 2012, 2015; Cerantola et al., 2017; Merlini et al., 2015, 2017; Lobanov et al., 2017). It is now of great interest to determine whether carbonates with sp^3-hybridized carbon form solid solutions with their silicate analogs and thus provide an alternative major host of carbon in the deeper mantle regions. Up to now, carbonates with CO_4-groups were synthesized at pressures >70 GPa, which led to the conclusion that only the deep lower mantle may provide the required thermodynamic conditions for their occurrence (Binck et al., 2020b; Boulard et al., 2011, 2012, 2015; Cerantola et al., 2017; Merlini et al., 2015, 2017; Lobanov et al., 2017).

Recent theoretical studies, however, have indicated that carbonate polymorphs in the system $CaO-CO_2$ which contain CO_4-groups may be stable at pressures and temperatures corresponding to the conditions of Earth's transition zone and uppermost lower mantle (Sagatova et al., 2020; Yao et al., 2018). Specifically, Yao et al., (2018) predicted that Ca_3CO_5-*Cmcm* and CaC_2O_5-*Pc* may be stable phases at pressures >11 and >33 GPa respectively, while Sagatova et al., (2020) found Ca_2CO_4-*Pnma* to be a stable phase at pressures >13 GPa.

While the phase diagram of $CaCO_3$ is fairly well constrained for the pressure and temperature conditions of Earth's upper and lower mantle (Bayarjargal et al., 2018; Gavryushkin et al., 2017; Ishizawa et al., 2013; Lobanov et al., 2017; Ono et al., 2007), experimental studies focusing on different compositions in the system CaO-CO_2 have not been reported up to now. In this study, we have used a multidisciplinary experimental and theoretical approach, which allowed us to verify the formation of calcium orthocarbonate (Ca_2CO_4-*Pnma*) at *p*, *T*-conditions of the Earth's transition zone and lower mantle. We report the experimentally determined crystal structure of calcium orthocarbonate (Ca_2CO_4-*Pnma*) and present the first experimental and theoretical Raman spectra of the new compound.

Experimental Methods

Preparation of high-pressure, high-temperature experiments

For low pressure and moderate temperature Raman spectroscopy and x-ray diffraction experiments (up to ~23 GPa and ~2300 K), Boehler-Almax type (Boehler, 2006) diamond anvil cells (DAC) were employed. Raman-compatible diamonds with low birefringence, ultra-low fluorescence and culets of 300-350 μm in diameter were inserted in WC seats. The opening angles of the cells were 48° and 70°, respectively. A BX-90 type DAC (Kantor et al., 2012) was used for high-pressure, high-temperature x-ray diffraction experiments (up to ~93 GPa and ~2500 K), with a 120 μm culet diamond inserted in a WC seat. Depending on the culet size, sample chambers of 60 - 175 μm in diameter were laser drilled in Re gaskets pre-indented to ~15 – 45 μm. The diamond anvil cells for the experiments at moderate pressures were loaded with natural $CaCO_3$ single crystals, surrounded by compacted CaO powder (analytical grade chemPUR 99.95%) and ruby pressure markers. The $CaCO_3$ single crystals had edge lengths ranging from ~15 - 60 μm. Before loading, CaO and $CaCO_3$ were dried for 48 h at 460°C, in order to remove surface moisture. The DAC employed for the high-pressure experiments was loaded with calcium azide (CaN_6) containing CaO and a nitrogen pressure transmitting medium.

Raman spectroscopy in the LH-DAC

Raman spectra were measured at the Institute of Geosciences at the Goethe Universität Frankfurt in 0.5 - 4 GPa steps upon compression and decompression covering a range between ambient pressure and ~23 GPa. A frequency doubled 532.14 nm Nd:YAG Oxxius laser (LCX 532S) was focused on the sample with a spot size of 6 μm. Spectra were collected in backscattering geometry, using a grating spectrometer (Acton, SP-2356) equipped with a CCD detector (Pixis 256E) and a microscope objective (Mitutoyo). The spectral resolution of the spectrometer is 3 cm^{-1} (Bayarjargal et al., 2018). The laser power was set to 430 mW and spectra were collected for 50 s in a frequency window of 100 - 1500 cm^{-1}, using a grating of 1800 grooves/mm. The estimated laser power on the sample was around ~250 mW. The pressure was determined before and after the Raman measurement, using the ruby reference scales for non-hydrostatic (Mao et al., 1978) conditions. The accuracy of our pressure determination by the ruby scale was ~2 GPa, while pressure gradients may have caused uncertainties up to 3 GPa during and after laser heating.

The sample was heated from both sides with a pulsed CO_2-laser (Diamond K-250 from Coherent, λ = 10.6 μm), reaching temperatures up to ~2300 K. For the determination we used the same set-up as for the Raman measurements, while the grating was set to 150 grooves/mm. In order to achieve coupling of the CO_2-laser from both sides of the sample, the laser power was set in a range between 1 - 6 W, depending on the pressure and the loading of the diamond anvil cell. The heating laser was focused on the sample so that the diameter of the heated area was around 25 μm, which nearly covered all of the single crystals. We moved the heating laser across the sample, while heating for about 5 min per position. The position of the Raman laser with respect to the heated areas on the sample was controlled using an optical camera. The thermal emission of the sample, as well as the Raman signal was measured with a spatial resolution of around 5 - 6 μm, i.e. the areas for the measurements were significantly smaller than the heating spots. The temperatures during laser heating were determined by the two-color pyrometer method, employing Planck and Wien fits (Benedetti et al., 2004). We assume a typical uncertainty associated with radiometric temperature measurements in LH-DACs of ~10 %.

High-pressure single-crystal x-ray diffraction

High pressure single-crystal x-ray diffraction (SC-XRD) data were acquired at the P02.2 and 13-IDD beamlines of PETRA III (DESY, Hamburg, Germany) and the Advanced Photon Source (APS, Chicago, USA), respectively. Two different phase assemblages were compressed up to ~20 and ~89 GPa at ambient temperature. The samples were laser-heated in a temperature range between ~1830 and ~2500 K once the cells had reached the desired pressures. The sample material of the low-pressure cell was heated using the CO_2-laser heating system described above. The high-pressure cell was heated using the double-sided YAG laser-heating system at the 13-

IDD beamline of the APS, with CaN_6 acting as the laser-absorber. Temperatures were measured using the thermal emission (Mezouar et al., 2017). The pressures inside the sample chambers were either determined using the ruby fluorescence method (Mao et al., 1978), or from the vibrational mode of the stressed diamond anvil (Akahama and Kawamura, 2006).

The synthesized polycrystalline samples were characterized upon compression and decompression by SC-XRD measurements. At the P02.2 beamline, a Perkin Elmer XRD 1621 detector was employed with an x-ray beam (λ = 0.2901 Å, or λ = 0.2887 Å, depending on the experiment) focused down to about 2 x 2 μm^2. At the GSECARS beamline, a Pilatus CdTe 1M detector was used along with an x-ray beam (λ = 0.2952 Å) focused down to 3 x 3 μm^2. On the polycrystalline samples, a full x-ray diffraction mapping of the sample chamber was performed after laser-heating in order to identify the most promising sample positions for a single-crystal data collection. On the locations where the most intense single-crystal reflections were detected, single-crystal data were acquired in step-scans of 0.5° from 36° to +36° ω and 5 s exposure time. The CrysAlisPro software (Rigaku Oxford Diffraction, 2018) was utilized for the single-crystal data analysis. To calibrate the instrumental model in the CrysAlisPro software, i.e., the sample to-detector distance, detector's origin, offsets of goniometer angles, and rotation of both x-ray beam and the detector around the instrument axis, a single crystal of orthoenstatite ($(Mg_{1.93}Fe_{0.06})(Si_{1.93}, Al_{0.06})O_6$, *Pbca* space group, a = 8.8117(2) Å, b = 5.18320(10) Å, and c = 18.2391(3) Å) was used. The same calibration crystal was used at all beamlines. The analysis procedure in the CrysAlisPro software includes the peak search, the removal of the diamond anvils' parasitic reflections and saturated pixels of the detector, finding reflections belonging to a unique single crystal, the unit cell determination and the data integration and absorption corrections. The crystal structures were then solved with SHELXT structure solution program

(Sheldrick, 2015) using intrinsic phasing and refined within the JANA2006 software (Petříček et al., 2014). CSD 2026976 contains the crystallographic data for Ca_2CO_4 at 89 GPa (Laniel, 2020). These data can be obtained free of charge from FIZ Karlsruhe via www.ccdc.cam.ac.uk/structures. Further structural data of Ca_2CO_4 at 20.1(2) GPa and 89.0(8) GPa are given in the associated CIF.

Density functional theory

In order to obtain theoretical Raman spectra, density functional perturbation theory (DFPT) calculations were performed employing the CASTEP code (Clark et al., 2005). The code is an implementation of Kohn-Sham DFT based on a plane wave basis set in conjunction with pseudopotentials. The plane wave basis set allows to achieve numerically converged results in a straightforward manner, as the convergence is controlled by a single adjustable parameter, the plane wave cut-off, which we set to 1020 eV. The norm-conserving pseudopotentials were generated 'on the fly' from the information provided in the CASTEP data base. These pseudopotentials have been tested extensively for accuracy and transferability (Lejaeghere et al., 2016). All calculations employed the GGA-PBE exchange-correlation functional (Perdew et al., 1996). The Brillouin zone integrals were performed using Monkhorst-Pack grids (Monkhorst and Pack, 1976) with spacings between grid points of less than 0.037 $Å^{-1}$. Geometry optimizations were defined as being converged when the energy change between iterations was $<0.5 \times 10^{-6}$ eV/atom, the maximal residual force was < 0.01 eV/Å, and the maximal residual stress was < 0.02 GPa. Phonon frequencies were obtained from density functional perturbation theory (DFPT) calculations. Raman intensities were computed using DFPT in the `2n + 1' theorem approach (Miwa, 2011) for a powder sample. We have shown in numerous studies that the relative intensities of Raman bands for carbonates are very well reproduced and predicted with this approach (Nguyen-Thanh et al., 2016; Biedermann et al., 2017; Bayarjargal et al., 2018; Binck et al., 2020a; Binck et al. 2020b). Reaction enthalpies were computed in the athermal limit by comparing the sum of the enthalpies of the reactants to those of the products at prescribed pressures.

Results

Crystal structure of Ca_2CO_4-*Pnma*

Our single-crystal diffraction measurements unequivocally show the appearance of a new set of diffraction spots upon laser-heating, which was indexed with an orthorhombic unit cell (space group *Pnma*). The structure was readily solved and refined for data sets obtained at 20.1(2) and 89.0(8) GPa (Supplementary[1] data). All other data sets between 10 and 93 GPa were successfully indexed with the same unit cell (Supplementary[1] data).

Ca_2CO_4-*Pnma* has 28 atoms ($Z = 4$ formula units) in the unit cell and is characterized by carbon that is coordinated by oxygen fourfold, forming isolated CO_4 tetrahedra. Ca atoms occupy two non-equivalent crystallographic positions and form CaO_9 and CaO_{11} polyhedra (Fig. 1). Geometric parameters of the crystal structure at 20.1(2) and 89.0(8) GPa are listed in Tab. 1.

The CO_4 tetrahedra share corners, edges and faces with the CaO_{11} polyhedra, but only share corners and edges with the CaO_9 polyhedra. The CaO_9 polyhedra are irregularly shaped, while the CaO_{11} polyhedra form fivefold-capped trigonal prisms (Sagatova et al., 2020). CaO_9 and CaO_{11} polyhedra are connected via their faces. Upon compression from 20.1(2) to 89.0(8) GPa, the overall unit cell volume decreases by ~20 %. The C-O bond lengths range from 1.378(14) to 1.386(7) Å at 20.1(2) GPa. They shorten by ~3 % when a pressure of 89.0(8) GPa is reached (C-

O bond range 1.323(16) - 1.381(11) Å). The volume of the CO_4 tetrahedra decreases by ~9 % from 20.1(2) GPa (V = 1.35 $Å^3$) to 89.0(8) GPa (V = 1.23 $Å^3$). The distortion of a coordination polyhedron can be defined by an index D, with $D = 1/n \sum_{i=1}^{n} \frac{|li-lav|}{|lav|}$, where l_i is the distance from the central atom to the ith coordinating atom and l_{av} is the average bond length (Baur, 1974). The distortion of the CO_4 polyhedra at 20.1(2) GPa is small with D = 0.002, and increases only slightly to 0.015 upon pressure increase to 89.0(8) GPa. The average bond lengths of the CaO_9 and CaO_{11} coordination polyhedra decrease from 2.360 to 2.174 Å and 2.532 to 2.338 Å over the same pressure range, corresponding to a pressure-induced volume decrease of 20.8 and 20.5 %, respectively.

In summary, our SC-XRD experiments demonstrated that CaO + $CaCO_3$ reacts at pressures as low as ~20 GPa and ~1830 K to form Ca_2CO_4. Further, the CaO in CaN_6 reacted with the diamond culet at ~89 GPa and ~2500 K to form Ca_2CO_4. The new phase formed in the experiments is a calcium orthocarbonate with a structure that has recently been predicted (Sagatova et al., 2020).

We calculated structural parameters for Ca_2CO_4-*Pnma* for pressures ranging from 0 to 100 GPa using density functional theory calculations. Our Mulliken population analysis of the C-O bonds clearly shows that all four C-O bonds in a CO_4 tetrahedron are similar, i.e. all four bonds have high populations of ~0.65 $e^-/Å^3$, indicative of covalent bonding. The calculated volume data were fitted using a third-order Birch-Murnaghan equation of state and are shown alongside experimental data (Fig. 2a). The extrapolated unit cell volume at ambient pressure is 302.0(3) $Å^3$ and the bulk modulus and its first pressure derivative are K_0 = 108(1) GPa and $K_0^{'}$ = 4.43(3), respectively. The experimentally determined unit cell dimensions closely resemble those obtained by DFT calculations derived in this work and by Sagatova et al., (2020) (Fig. 2a and b). The

DFT-calculated volumes of the CO_4, CaO_9 and CaO_{11} polyhedra were further fitted using third-order Birch-Murnaghan equations of state and are shown together with the experimental volumes of the solved crystal structures (Fig. 3 and Supplementary[1] data). The bulk modulus of the CO_4 groups is 360(38) GPa with $K_0^{'}$ = 6.70(12) and V_0 = 1.433(5) Å^3. For the CaO_9 and CaO_{11} polyhedra, the bulk moduli are 99(3) GPa and 106(3) GPa with $K_0^{'}$ = 4.30(8) and V_0 = 29.32(8), as well as $K_0^{'}$ = 4.31(9) and 40.09(11) Å^3, respectively.

Experimental and theoretical Raman spectra of Ca_2CO_4-*Pnma*

Raman spectra of CaO + $CaCO_3$ were measured upon cold compression up to 22.8(2) GPa. Raman signals of a sequence of meta-stable high-pressure polymorphs are expected when calcite is used as $CaCO_3$ precursor instead of aragonite (Bayarjargal et al., 2018; Koch-Müller et al., 2016). CaO-$Fm\overline{3}m$, on the other hand, is known to be Raman inactive and should not contribute to the measured signal. We obtained $CaCO_3$-III at around ~6 GPa, which eventually transformed to $CaCO_3$-VI at above ~15 GPa (Supplementary[1] data). We increased the pressure to ~23 GPa before laser heating. When heating the $CaCO_3$-VI single crystals to ~1830 and to ~2255 K in two distinct experiments, they reacted immediately with the surrounding CaO-$Fm\overline{3}m$. In both runs, the pressure after heating dropped by approximately 1.6 - 2.7 GPa. Raman spectra that have been obtained after quenching the sample to ambient temperatures show well-resolved new features (Fig. 4), which cannot be explained by the Raman spectra of $CaCO_3$-VI or of aragonite (Supplementary[1] data). At 19.9(4) GPa, the most prominent feature of the newly synthesized phase is a strong Raman band at 996.4 cm^{-1} (Fig. 4). Furthermore, at least eight new Raman bands are observable in a range of 557-774 cm^{-1}, and more than twelve new modes appear in the low frequency range between 121-399 cm^{-1}. We observe $CaCO_3$-VI in the non-heated areas, which demonstrates the localized increase of temperature upon laser heating. In both runs, we were not able to find any evidence for the presence of aragonite, suggesting a strong reactivity in the CaO-$CaCO_3$ system if sufficient energy is provided.

According to group theory, forty-two Raman active modes are expected for Ca_2CO_4-*Pnma*: $\Gamma_{Raman} = 13A_g+8B_{1g}+13B_{2g}+8B_{3g}$. The most prominent characteristic of Ca_2CO_4-*Pnma* is an intra-molecular Raman band that is appearing around 1000 cm^{-1}. Raman bands in the same frequency interval have been shown to be distinctive of the intra-molecular vibrations of the CO_4 tetrahedra in $CaCO_3$-$P2_1/c$ (Lobanov et al., 2017) and $MgCO_3$-C2/m (Binck et al., 2020b). Fig. 5 demonstrates a good match between the theoretical and experimental Raman modes indicating that Ca_2CO_4-*Pnma* is the only carbonate with sp^3-hybridized carbon present in the sample. We observe at least twenty-three experimental Raman modes which can be assigned to the theoretical spectrum at 20 GPa (Fig. 5). Missing Raman bands are due to the resolution of the spectrometer or high background of the diamonds. A calculated Raman spectrum of Ca_2CO_4-*Pnma* at 83 GPa implies positive Grüneisen-parameters for all modes (Supplementary[1] data). According to previous calculations, Ca_2CO_4-*Pnma* is thought to decompose below 10 GPa (Sagatova et al., 2020). We were able to acquire Raman spectra of Ca_2CO_4-*Pnma* down to 4.1(2) GPa. Below that pressure the Raman spectra do not exhibit any of the characterizing features of Ca_2CO_4 anymore (Supplementary[1] data). Instead, at ambient conditions, a diffuse spectrum clearly showing the lattice vibrations of the CO_3-stretching mode is present (Supplementary[1] data). Since the distinctive features of crystalline carbonate are absent, we infer that its amorphization has taken place due to the cold pressure relaxation. As the decomposition may require an activation energy, the actual stability field of Ca_2CO_4-*Pnma* currently remains unknown.

Discussion and Implications

Our results demonstrate that calcium orthocarbonate (Ca_2CO_4-*Pnma*) can be formed at the *p, T*-conditions of Earth's upper transition zone at ~20 GPa and ~1830 K and can persist to at least the mid-lower mantle conditions (up to ~93 GPa and ~2500 K). During the investigation of the CaO-$CaCO_3$ system, we neither found indications for the previously predicted Ca_3CO_5-*Cmcm* phase and its high-pressure polymorphs (Sagatova et al., 2020; Yao et al., 2018), nor for the predicted meta-stable Ca_2CO_4-$P2_1/m$ phase (Yao et al., 2018).

Our constraints on the formation conditions of Ca_2CO_4-*Pnma* imply that some compounds in the CaO-CO_2 system may have comparatively low sp^2-sp^3 transition pressures, corresponding to lower upper mantle conditions. This stands in strong contrast to the sp^2-sp^3 crossover of pure $CaCO_3$, which was observed at pressures >100 GPa (Lobanov et al., 2017; Oganov et al., 2006; Ono et al., 2007; Pickard and Needs, 2015). Although the solubility of carbon into major mantle minerals has been shown to be low (Shcheka et al., 2006), the sp^2-sp^3 transition in carbonates may have a significant impact on the silicate-carbonate equilibria and thus the potential for carbonates to exist in the mantle. Such effects can now be studied in the CaO-CO_2 system at comparatively low pressures with large-volume presses.

A topological analogy of Ca_2CO_4-*Pnma* with the silicates larnite β-Ca_2SiO_4 (Barbier et al., 1985) and flamite α'_H-Ca_2SiO_4 (Rashchenko et al., 2019) has been reported (Sagatova et al., 2020). Carbon substitution of SiO_4-groups by CO_4-groups is, however, unlikely as the former are more voluminous by a factor of ~2 than the latter (e.g. Hugh-Jones et al., 1997; Kudo and Takéuchi, 1985; Milman et al., 2001; Smyth and Bish, 1988 and references therein). Also, the compressibility of isolated CO_4 tetrahedra (K_0 ~360 GPa) is smaller than that of SiO_4 tetrahedra (K_0 ~ 300 GPa) which, based on crystal chemical considerations is the expected behavior due to the smaller cation radius of C. However, it is now worthwhile to explore the phase stabilities of compounds in which CO_4 groups and SiO_6-octahedra may coexist.

We investigated whether sp^3-hybridized calcium orthocarbonate can coexist with silicates in the mantle. While at the *p, T*-conditions of the transition zone and upper lower mantle, $CaCO_3 + SiO_2$ were shown to form $CaSiO_3 + CO_2$ (Li et al., 2018), our DFT-calculations at 20, 30 and 40 GPa show, that $Ca_2CO_4 + 2SiO_2$ are more stable than $2CaSiO_3 + CO_2$ (Fig. 6). This implies that Ca_2CO_4-*Pnma* could exist together with silica at the *p, T*-conditions of the transition zone and upper lower mantle. In fact, the presence of $CaCO_3$ inclusions in super deep diamonds derived from the transition zone or the lower mantle (Brenker et al., 2007; Kaminsky et al., 2016) is inconsistent with the assumption that $CaCO_3$ will always react with the surrounding mantle.

Isotopic signatures (Harte, 2010; Tappert et al., 2005) and carbonate inclusions in diamonds (Brenker et al., 2007; Kaminsky et al., 2016) suggest that diamonds may form during 'redox freezing', i.e. when the oxidized carbonate-bearing subducting slab has reached the more reduced transition zone or the lower mantle, and releases carbonate and/or carbonatitic melts which reduce oxidized carbon to diamond (Rohrbach et al., 2011; Stagno et al., 2013). The inverse scenario called 'redox melting' occurs when reduced carbon-bearing rocks are lifted up above the 660 km discontinuity of the transition zone due to the upwelling mantle (Rohrbach et al., 2011; Stagno et al., 2013). In this case, carbonate and/or carbonatitic melts form due to re-oxidation of diamond. Our results show that Ca_2CO_4-*Pnma* may form during such redox processes. Diamonds that have formed during redox melting could initially conserve calcium orthocarbonate. These orthocarbonates would transform or decompose once the diamond is elevated above the base of thick continental crust and could then only be identified by the decomposition products. Indications of the presence of calcium-bearing inclusions such as CaO, CaF_2 and $Ca(OH)_2$ in diamond have been found in the presence of CO_3-groups (Dobrzhinetskaya et al., 2007). Such a phase assemblage would be consistent with the expected remnants of decomposed Ca_2CO_4-*Pnma*.

Acknowledgements

The authors acknowledge funding by the Deutsche Forschungsgemeinschaft (DFG)-Germany (FOR2125/CarboPaT, BA4020, WI1232). The `2n + 1' Raman theorem in CASTEP was developed under grant EP/I030107/1. D.L. thanks the Alexander von Humboldt Foundation for financial support. DESY (Hamburg, Germany), a member of the Helmholtz Association (HGF) is acknowledged for the provision of experimental facilities. Portions of this work were performed at GeoSoilEnviroCARS (The University of Chicago, Sector 13), Advanced Photon Source (APS), Argonne National Laboratory. GeoSoilEnviroCARS is supported by the National Science Foundation - Earth Sciences (EAR - 1634415) and Department of Energy- GeoSciences (DE-FG02-94ER14466). This research used resources of the Advanced Photon Source, a U.S. Department of Energy (DOE) Office of Science User Facility operated for the DOE Office of Science by Argonne National Laboratory under Contract No. DE-AC02-06CH11357.

References cited

Akahama, Y., Kawamura, H. (2006) Pressure calibration of diamond anvil Raman gauge to 310 GPa, Journal of Applied Physics, 100, 043516.

Barbier, J., Hyde, B. (1985) The structures of the polymorphs of dicalcium silicate, Ca_2SiO_4, Acta Crystallographica Section B: Structural Science, 41, 383-390.

Baur, W. (1974) The geometry of polyhedral distortions. Predictive relationships for the phosphate group, Acta Crystallographica Section B: Structural Crystallography and Crystal Chemistry, 30, 1195-1215.

Bayarjargal, L., Fruhner, C.-J., Schrodt, N., Winkler, B., (2018) $CaCO_3$ phase diagram studied with Raman spectroscopy at pressures up to 50 GPa and high temperatures and DFT modeling, Physics of the Earth and Planetary Interiors, 281, 31-45.

Benedetti, L.R., Loubeyre, P. (2004) Temperature gradients, wavelength-dependent emissivity, and accuracy of high and very-high temperatures measured in the laser-heated diamond cell, High Pressure Research, 24, 423-445.

Biedermann, N., Speziale, S., Winkler, B., Reichmann, H. J., Koch-Müller, M., Heide, G. (2017) High-pressure phase behavior of $SrCO_3$: an experimental and computational Raman scattering study, Physics and Chemistry of Minerals, 44, 335-343.

Binck, J., Chariton, S., Stekiel, M., Bayarjargal, L., Morgenroth, W, Milman, V., Dubrovinsky, L., Winkler, B. (2020a) High-pressure, high-temperature phase stability of iron-poor dolomite and the structures of dolomite-IIIc and dolomite-V, Physics of the Earth and Planetary Interiors, 299, 106403.

Binck, J., Bayarjargal, L., Lobanov, S.S., Morgenroth, W., Luchitskaia, R., Pickard, C.J., Milman, V., Refson, K., Jochym, D.B., Byrne, P., Winkler, B. (2020b) Phase stabilities of $MgCO_3$ and $MgCO_3$-II studied by Raman spectroscopy, x-ray diffraction, and density functional theory calculations, Physical Review Materials, 4, 055001.

Birch, F. (1947) Finite elastic strain of cubic crystals, Physical review, 71, 809.

Boehler, R. (2006) New diamond cell for single-crystal X-ray diffraction, Review of Scientific Instruments, 77, 115103.

Boulard, E., Gloter, A., Corgne, A., Antonangeli, D., Auzende, A.L., Perrillat, J.P., Guyot, F., Fiquet, G. (2011) New host for carbon in the deep Earth, Proceedings of the National Academy of Sciences, 108, 5184-5187.

Boulard, E., Menguy, N., Auzende, A.L., Benzerara, K., Bureau, H., Antonangeli, D., Corgne, A., Morard, G., Siebert, J., Perrillat, J.P., Guyot, F., Fiquet, G. (2012) Experimental investigation of the stability of Fe-rich carbonates in the lower mantle, Journal of Geophysical Research: Solid Earth, 117.

Boulard, E., Pan, D., Galli, G., Liu, Z., Mao, W.L. (2015) Tetrahedrally coordinated carbonates in Earth's lower mantle, Nature communications, 6, 6311.

Brenker, F.E., Vollmer, C., Vincze, L., Vekemans, B., Szymanski, A., Janssens, K., Szaloki, I., Nasdala, L., Joswig, W., Kaminsky, F. (2007) Carbonates from the lower part of transition zone or even the lower mantle, Earth and Planetary Science Letters, 260, 1-9.

Caracas, R., Wentzcovitch, R., Price, G.D., Brodholt, J. (2005) $CaSiO_3$ perovskite at lower mantle pressures, Geophysical Research Letters, 32.

Caracas, R., Wentzcovitch, R.M. (2006) Theoretical determination of the structures of $CaSiO_3$ perovskites, Acta Crystallographica Section B: Structural Science, 62, 1025-1030.

Cerantola, V., Bykova, E., Kupenko, I., Merlini, M., Ismailova, L., Mc-Cammon, C., Bykov, M., Chumakov, A.I., Petitgirard, S., Kantor, I., Svitlyk, V., Jacobs, J., Hanand, M., Mezouar, M., Prescher, C., Rüffer, R., Prakapenka, V.B., Dubrovinsky, L. (2017) Stability of iron bearing carbonates in the deep Earth's interior, Nature Communications, 8, 15960.

Chariton, S., Bykov, M., Bykova, E., Koemets, E., Fedotenko, T., Winkler, B., Hanand, M., Prakapenka, V.B., Greenberg, E., McCammon, C., Dubrovinsky, L. (2020) The crystal structures of Fe-bearing $MgCO_3$ *sp*^{2}-and *sp*^{3}-carbonates at 98 GPa from single-crystal X-ray diffraction using synchrotron radiation, Acta Crystallographica Section E: Crystallographic Communications, 76, 715-719.

Clark, S.J., Segall, M.D., Pickard, C.J., Hasnip, P.J., Probert, M.I., Refson, K., Payne, M.C. (2005) First principles methods using CASTEP, Zeitschrift für Kristallographie-Crystalline Materials, 220, 567-570.

Clift, P.D., (2017) A revised budget for Cenozoic sedimentary carbon subduction, Reviews of Geophysics, 55, 97-125.

Dobrzhinetskaya, L.F., Wirth, R., Green, H.W. (2007) A look inside of diamond-forming media in deep subduction zones, Proceedings of the National Academy of Sciences, 104, 9128-9132.

Gavryushkin, P.N., Martirosyan, N.S., Inerbaev, T.M., Popov, Z.I., Rashchenko, S.V., Likhacheva, A.Y., Lobanov, S.S., Goncharov, A.F., Prakapenka, V.B., Litasov, K.D. (2017) Aragonite-II and $CaCO_3$-VII: New high pressure, high-temperature polymorphs of CaCO3, Crystal Growth & Design, 17, 6291-6296.

Gonzalez-Platas, J., Alvaro, M., Nestola, F., Angel, R. J. (2016) EosFit7-GUI: A new GUI tool for equation of state calculations, analyses and teaching. Journal of Applied Crystallography, 49, 1377-1382.

Han, Y., Liu, J., Huang, L., He, X., Li, J. (2019) Predicting the phase diagram of solid carbon dioxide at high pressure from first principles, npj Quantum Materials, 4, 1-7.

Harte, B. (2010) Diamond formation in the deep mantle: the record of mineral inclusions and their distribution in relation to mantle dehydration zones, Mineralogical Magazine, 74, 189-215.

Hirschmann, M.M., (2018) Comparative deep earth volatile cycles: The case for c recycling from exosphere/mantle fractionation of major (H_2O, C, N) volatiles and from H_2O/Ce, CO_2/Ba, and CO_2/Nb exosphere ratios, Earth and Planetary Science Letters, 502, 262-273.

Hugh-Jones, D., Chopelas, A., Augel, R. (1997) Tetrahedral compression in (Mg,Fe)SiO_3 orthopyroxenes, Physics and Chemistry of Minerals, 24, 301-310.

Ishizawa, N., Setoguchi, H., Yanagisawa, K. (2013) Structural evolution of calcite at high temperatures: Phase V unveiled, Scientific Reports, 3, 2832.

Kaminsky, F.V., Ryabchikov, I.D., Wirth, R. (2016) A primary natrocarbonatitic association in the Deep Earth, Mineralogy and Petrology, 110, 387-398.

Kantor, I., Prakapenka, V., Kantor, A., Dera, P., Kurnosov, A., Sinogeikin, S., Dubrovinskaia, N., Dubrovinsky, L. (2012) BX90: A new diamond anvil cell design for X-ray diffraction and optical measurements, Review of Scientific Instruments, 83, 125102.

Kelemen, P.B., Manning, C.E., (2015) Reevaluating carbon fluxes in subduction zones, what goes down, mostly comes up, Proceedings of the National Academy of Sciences, 112, E3997-E4006.

Komabayashi, T., Hirose, K., Sata, N., Ohishi, Y., Dubrovinsky, L.S. (2007) Phase transition in $CaSiO_3$ perovskite, Earth and Planetary Science Letters, 260, 564-569.

Koch-Müller, M., Jahn, S., Birkholz, N., Ritter, E., Schade, U. (2016) Phase transitions in the system $CaCO_3$ at high P and T determined by in situ vibrational spectroscopy in diamond anvil cells and first-principles simulations, Physics and Chemistry of Minerals, 43, 545-561.

Kudoh, Y., Takéuchi, Y. (1985) The crystal structure of forsterite Mg_2SiO_4 under high pressure up to 149 kb, Zeitschrift für Kristallographie-Crystalline Materials, 171, 291-302.

Laniel, D. (2020) CCDC 2026976: Experimental Crystal Structure Determination. CCDC, FIZ Karlsruhe. DOI: 10.5517/ccdc.csd.cc2617bv

Lejaeghere, K., Bihlmayer, G., Björkman, Blaha, T.P., Blügel, S., Blum, V., Caliste, D., Castelli, I.E., Clark, S.J., Dal Corso, A., et al. (2016) Reproducibility in density functional theory calculations of solids, Science, 351.

Li, X., Zhang, Z., Lin, J.-F., Ni, H., Prakapenka, V.B., Mao, Z. (2018) New high-pressure phase of $CaCO_3$ at the topmost lower mantle: Implication for the deep-mantle carbon transportation, Geophysical Research Letters, 45, 1355-1360.

Lobanov, S.S., Dong, X., Martirosyan, N.S., Samtsevich, A.I., Stevanovic, V., Gavryushkin, P.N., Litasov, K.D., Greenberg, E., Prakapenka, V.B., Oganov A.R., Goncharov A.F. (2017) Raman spectroscopy and x-ray diffraction of sp^3 $CaCO_3$ at lower mantle pressures, Physical Review B, 96, 104101.

Lu, C., Miao, M., Ma, Y. (2013) Structural evolution of carbon dioxide under high pressure, Journal of the American Chemical Society, 135, 14167-14171.

Maeda, F., Ohtani, E., Kamada, S., Sakamaki, T., Hirao, N., Ohishi, Y. (2017) Diamond formation in the deep lower mantle: A high-pressure reaction of $MgCO_3$ and SiO_2, Scientific reports, 7, 40602.

Mao, H., Bell, P., Shaner, J.T., Steinberg, D. (1978) Specific volume measurements of Cu, Mo, Pd, and Ag and calibration of the ruby R1 fluorescence pressure gauge from 0.06 to 1 Mbar, Journal of applied physics, 49, 3276-3283.

Martirosyan, N., Yoshino, T., Shatskiy, A., Chanyshev, A., Litasov, K. (2016) The $CaCO_3$-Fe interaction: Kinetic approach for carbonate subduction to the deep Earth's mantle, Physics of the Earth and Planetary Interiors, 259, 1-9.

McKenzie, N.R., Horton, B.K., Loomis, S.E., Stockli, D.F., Planavsky, N.J., Lee, C.-T.A., (2016) Continental arc volcanism as the principal driver of icehouse-greenhouse variability, Science, 352, 444-447.

Merlini, M., Hanand, M., Salamat, A., Petitgirard, S., Müller, H. (2015) The crystal structures of $Mg_2Fe_2C_4O_{13}$, with tetrahedrally coordinated carbon, and $Fe_{13}O_{19}$, synthesized at deep mantle conditions, American Mineralogist, 100, 2001-2004.

Merlini, M., Cerantola, V., Gatta, G.D., Gemmi, M., Hanand, M., Kupenko, I., Lotti, P., Müller, H., Zhang, L., (2017) Dolomite-IV: Candidate structure for a carbonate in the Earth's lower mantle, American Mineralogist, 102, 1763-1766.

Mezouar, M., Giampaoli, R., Garbarino, G., Kantor, I., Dewaele, A., Weck, G., Boccato, S., Svitlyk, V., Rosa, A., Torchio R., Mathon, O., Hignette, O., Bauchau, S. (2017) Methodology for in situ synchrotron X-ray studies in the laser heated diamond anvil cell, High Pressure Research, 37, 170-180.

Milman, V., Akhmatskaya, E., Nobes, R., Winkler, B., Pickard, C., White, J. (2001) Systematic ab initio study of the compressibility of silicate garnets, Acta Crystallographica Section B: Structural Science, 57, 163-177.

Miwa, K. (2011) Prediction of raman spectra with ultrasoft pseudopotentials, Physical Review B, 84, 094304.

Monkhorst, H.J., Pack, J.D. (1976) Special points for Brillouin-zone integrations, Physical review B, 13, 5188.

Nguyen-Thanh, T., Bosak, A., Bauer, J. D., Luchitskaia, R., Refson, K., Milman, V., Winkler, B. (1976) Lattice dynamics and elasticity of $SrCO_3$, Journal of Applied Crystallography, 49, 1982-1990.

Oganov, A.R., Glass, C.W., Ono, S. (2006) High-pressure phases of $CaCO_3$: Crystal structure prediction and experiment, Earth and Planetary Science Letters, 241, 95-103.

Ono, S., Kikegawa, T., Ohishi, Y. (2007) High-pressure transition of $CaCO_3$, American Mineralogist, 92, 1246-1249.

Palyanov, Y.N., Bataleva, Y.V., Sokol, A.G., Borzdov, Y.M., Kupriyanov, I.N., Reutsky, V.N., Sobolev, N.V. (2013) Mantle-slab interaction and redox mechanism of diamond formation, Proceedings of the National Academy of Sciences, 110, 20408-20413.

Perdew, J.P., Burke, K., Ernzerhof, M. (1996) Generalized gradient approximation made simple, Physical review letters, 77, 3865.

Petříček, V., Důsek, M., Palatinus, L. (2014) Crystallographic computing system JANA2006: General features, Zeitschrift für Kristallographie-Crystalline Materials, 229, 345 352.

Pickard, C.J., Needs R.J. (2015) Structures and stability of calcium and magnesium carbonates at mantle pressures, Physical Review B, 91, 104101.

Rashchenko, S.V., Seryotkin, Y.V., Sokol, E.V., Kokh, S.N. (2019) Incommensurately modulated crystal structure of flamite-natural analogue of α'_H-Ca_2SiO_4, Acta Crystallographica Section B: Structural Science, Crystal Engineering and Materials 75.

Rigaku, O. D., and CrysAlis, P. R. O. (2018) Rigaku Oxford Diffraction. Yarnton, England.

Ridgwell, A., (2005) A Mid Mesozoic Revolution in the regulation of ocean chemistry, Marine Geology, 217, 339-357.

Rohrbach, A., Schmidt, M.W. (2011) Redox freezing and melting in the Earth's deep mantle resulting from carbon-iron redox coupling, Nature, 472, 209-212.

Sagatova, D., Shatskiy, A., Sagatov, N., Gavryushkin, P.N., Litasov, K. D. (2020) Calcium orthocarbonate, Ca_2CO_4-*Pnma*: A potential host for subducting carbon in the transition zone and lower mantle, Lithos, 370, 105637.

Shcheka, S.S., Wiedenbeck, M., Frost, D.J., Keppler, H. (2006) Carbon solubility in mantle minerals, Earth and Planetary Science Letters, 245, 730-742.

Sheldrick, G.M. (2015) SHELXT - Integrated space-group and crystal structure determination, Acta Crystallographica Section A, 71, 3-8.

Smyth, J.R., Bish, D.L. (1988) Crystal structures and cation sites of the rock-forming minerals, Allen & Unwin Boston, p. 332.

Stagno, V., Tange, Y., Miyajima, N., McCammon, C., Irifune, T., Frost, D. (2011) The stability of magnesite in the transition zone and the lower mantle as function of oxygen fugacity, Geophysical Research Letters, 38.

Stagno, V., Ojwang, D.O., McCammon, C.A., Frost, D.J. (2013) The oxidation state of the mantle and the extraction of carbon from Earth's interior, Nature, 493, 84.

Tappert, R., Stachel, T., Harris, J.W., Muehlenbachs, K., Ludwig, T., Brey, G.P. (2005) Subducting oceanic crust: The source of deep diamonds, Geology, 33, 565-568.

Wallmann, K., (2001) Controls on the Cretaceous and Cenozoic evolution of seawater composition, atmospheric CO_2 and climate, Geochimica et Cosmochimica Acta, 65, 3005 3025.

Walter, M.J., Kohn, S.C., Araujo, D., Bulanova, G.P., Smith, C.B., Gaillou, E., Wang, J., Steele, A., Shirey, S.B. (2011) Deep mantle cycling of oceanic crust: Evidence from diamonds and their mineral inclusions, Science, 334, 54-57.

Yao, X., Xie, C., Dong, X., Oganov, A.R., Zeng, Q. (2018) Novel high-pressure calcium carbonates, Physical Review B, 98, 014108.

Figure captions

Figure 1. Structure of calcium orthocarbonate (Ca_2CO_4-*Pnma*) at ~20 GPa. Carbon atoms appear to no longer be coordinated by oxygen threefold, but form isolated CO_4 tetrahedra. The Ca atoms occupy two different sites, and they form CaO_9 (orange) and CaO_{11} (green) polyhedra.

Figure 2. a) Pressure-dependence of the unit-cell volume of Ca_2CO_4-*Pnma*. The DFT data were fitted using a third-order Birch-Murnaghan EOS (Gonzalez-Platas et al., 2016; Birch, 1947) using the *EoS-FIT7-GUI* program (Gonzalez-Platas et al., 2016). **b)** Linear fits (dashed lines) to the pressure dependence of DFT lattice parameters. Colors correspond to the a (red), b (green) and c (blue) lattice parameters. Filled and open squares correspond to experimental data obtained upon compression and decompression, respectively. Filled triangles correspond to DFT-calculated data points. Stars correspond to the predicted lattice parameters of Ca_2CO_4-*Pnma* at 25 GPa as obtained by Sagatova et al., (2020).

Figure 3. Pressure-dependence of the CO_4 tetrahedron volume of Ca_2CO_4-*Pnma*. The DFT data were fitted using a third-order Birch-Murnaghan EOS (Gonzalez-Platas et al., 2016; Birch, 1947) using the *EoS-FIT7-GUI* program (Gonzalez-Platas et al., 2016).

Figure 4. Experimental Raman spectra obtained in the CaO-$CaCO_3$ system. At ambient conditions, only $CaCO_3$ with calcite structure ($R\overline{3}c$) is Raman-active, which upon cold

compression to 21.5(2) GPa has the $CaCO_3$-VI structure ($P\overline{1}$). After heating to ~2255 K and quenching to ambient temperature, $CaCO_3$-VI has reacted with CaO, forming calcium orthocarbonate Ca_2CO_4 with the *Pnma* space group.

Figure 5. Comparison of experimental (temperature quenched from ~2255 K) versus theoretical Raman spectra of Ca_2CO_4-*Pnma* at ~20 GPa. The calculated frequencies were multiplied by a scaling factor of 1.04.

Figure 6. Pressure-dependence of the reaction enthalpy ΔH for the reaction $Ca_2CO_4 + 2SiO_2 \rightleftharpoons 2CaSiO_3 + CO_2$. Negative values indicate that the phase assemblage on the left-hand side of the equation is stable. Cross symbols represent calculated values, the solid red line is a linear fit to these values, while the dashed red parts indicate an extrapolation. The values plotted are for CO_2-V and orthorhombic $CaSiO_3$-perovskite. Using either CO_2-III or CO_2-IV (Han et al., 2019; Lu et al., 2013) would stabilize Ca_2CO_4 further by ~0.2 eV. The enthalpy difference between cubic and orthorhombic $CaSiO_3$ (Caracas et al., 2005, 2006; Komabayashi et al., 2007) is negligible in the present context.

Table 1. Structural parameters of Ca_2CO_4-*Pnma* at 20 and 89 GPa. Distances are in *d*(Å), angles in ∠(°).

Pressure (GPa)	Group	Min	Max	Average
20.1(2)	*d*(C-O)	1.378(14)	1.386(7)	1.383
	∠(O-C-O)	107.5(5)	112.9(6)	110.3
	d(Ca1-O)	2.227(8)	2.601(2)	2.360
	d(Ca2-O)	2.258(9)	2.893(6)	2.532
89.0(8)	*d*(C-O)	1.323(16)	1.381(11)	1.340
	∠(O-C-O)	107.4(6)	116.0(9)	109.5

d(Ca1-O)	2.088(8)	2.329(4)	2.174
d(Ca2-O)	2.129(6)	2.559(10)	2.338

561

Fig. 1

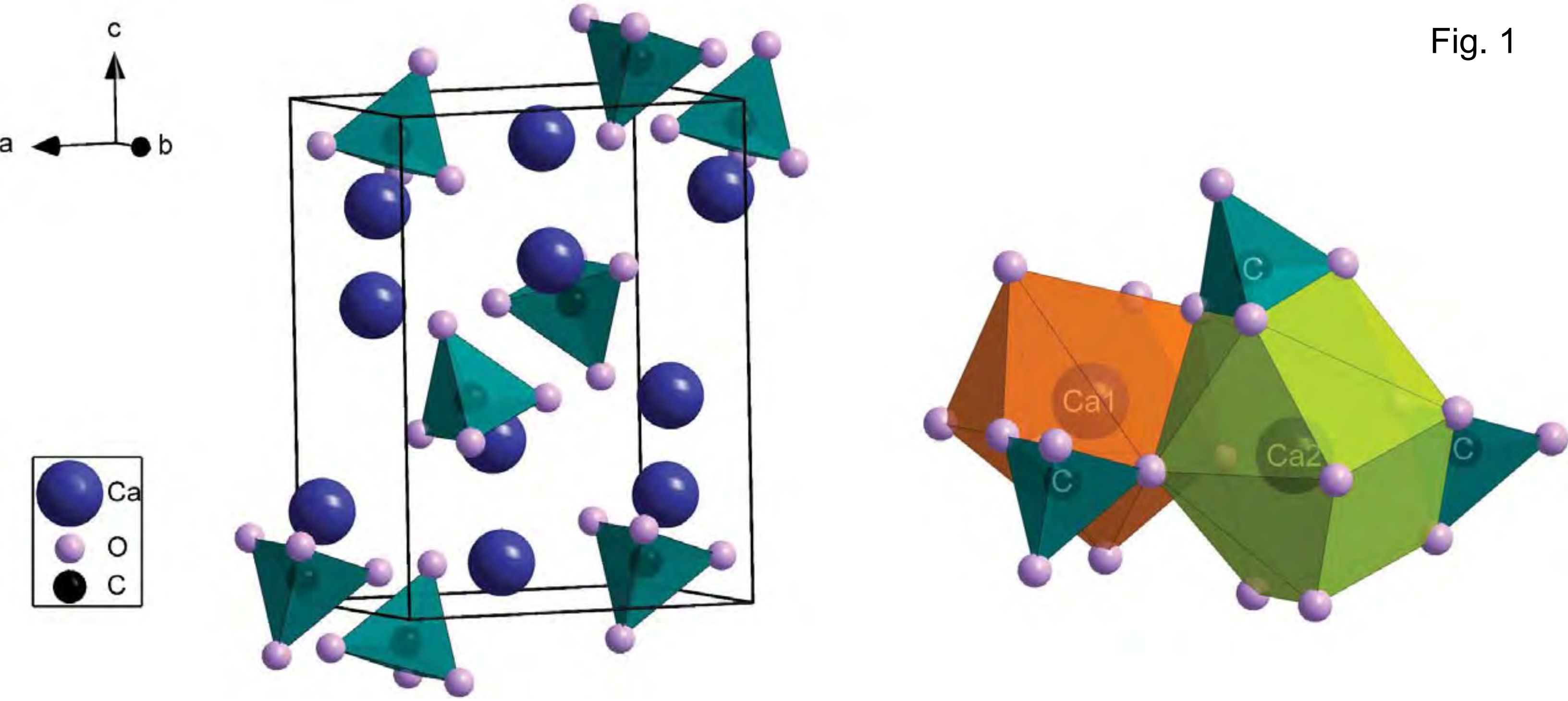

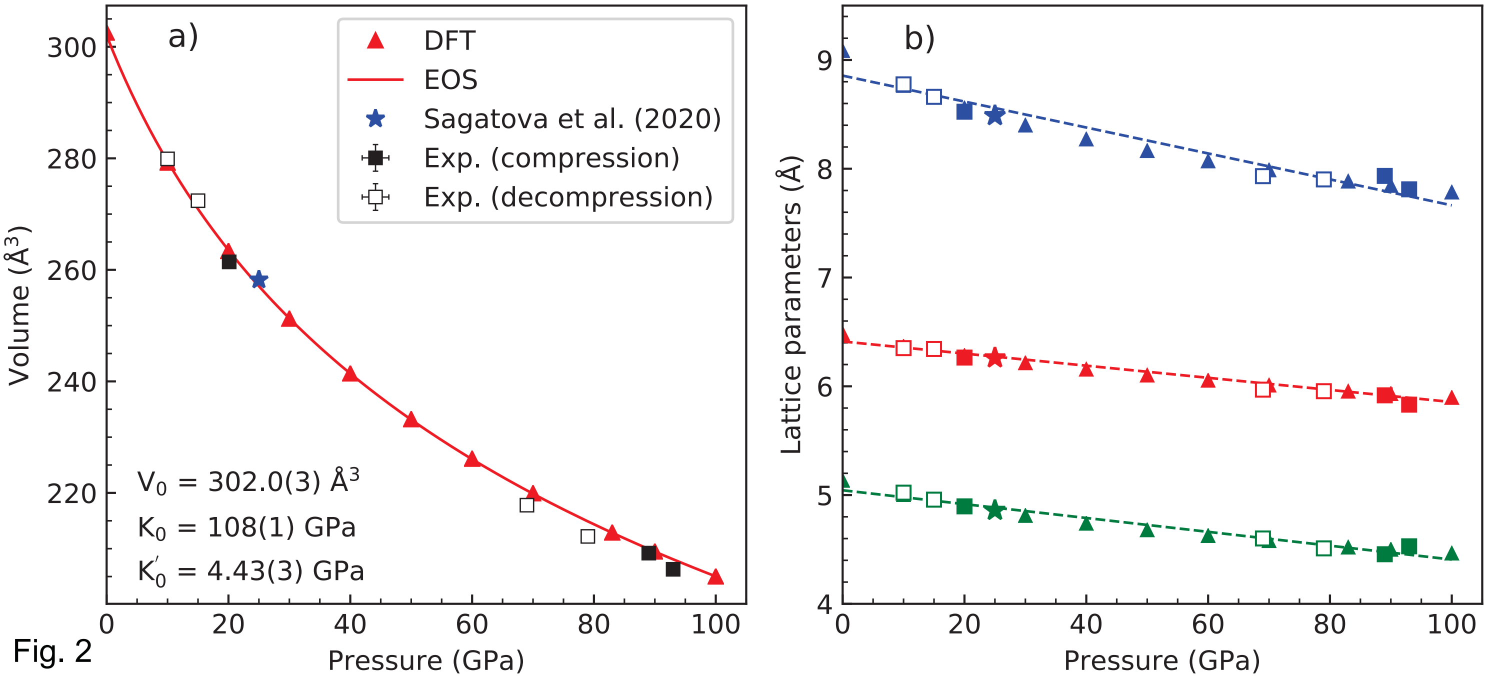
a)
DFT
EOS
Sagatova et al. (2020)
Exp. (compression)
Exp. (decompression)
Volume (Å^3)
300
280
260
240
220
V_0 = 302.0(3) Å^3
K_0 = 108(1) GPa
K_0' = 4.43(3) GPa
0
20
40
60
80
100
Pressure (GPa)
b)
Lattice parameters (Å)
9
8
7
6
5
4
0
20
40
60
80
100
Pressure (GPa)

Fig. 2

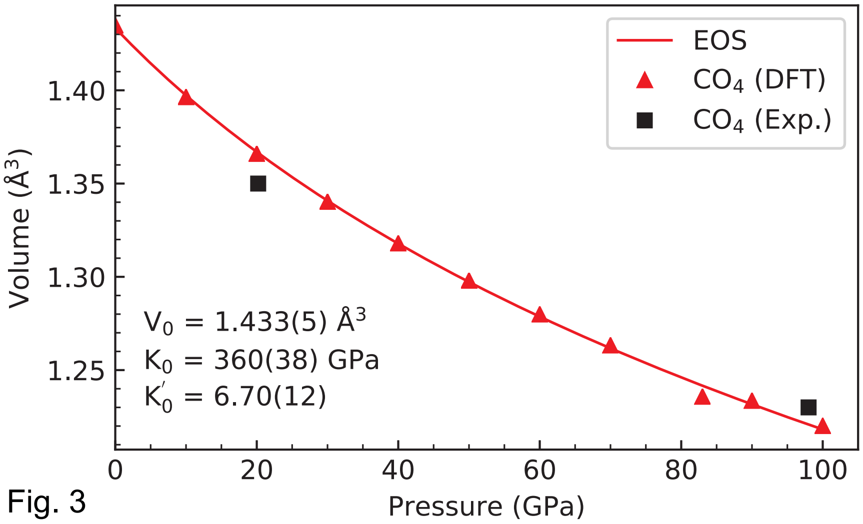
EOS
CO_4 (DFT)
CO_4 (Exp.)
V_0 = 1.433(5) Å^3
K_0 = 360(38) GPa
K_0' = 6.70(12)
Volume (Å^3)
Pressure (GPa)
1.40
1.35
1.30
1.25
0
20
40
60
80
100

Fig. 3

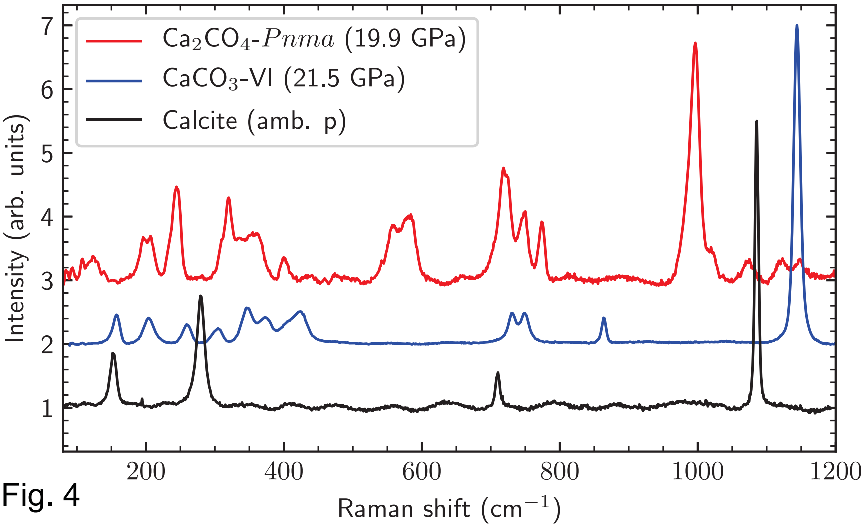
Ca_2CO_4-$Pnma$ (19.9 GPa)
$CaCO_3$-VI (21.5 GPa)
Calcite (amb. p)
Intensity (arb. units)
1
2
3
4
5
6
7
200
400
600
800
1000
1200
Raman shift (cm^{-1})

Fig. 4

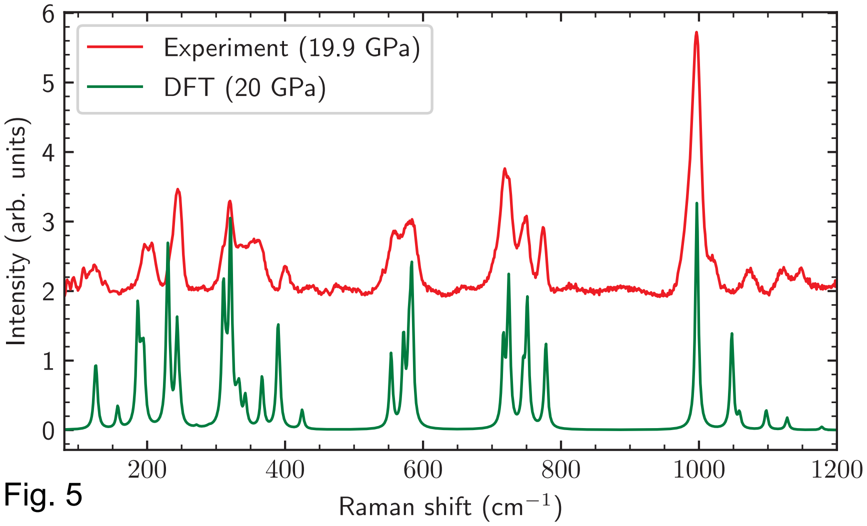
Experiment (19.9 GPa)
DFT (20 GPa)
Intensity (arb. units)
0
1
2
3
4
5
6
200
400
600
800
1000
1200
Raman shift (cm^{-1})

Fig. 5

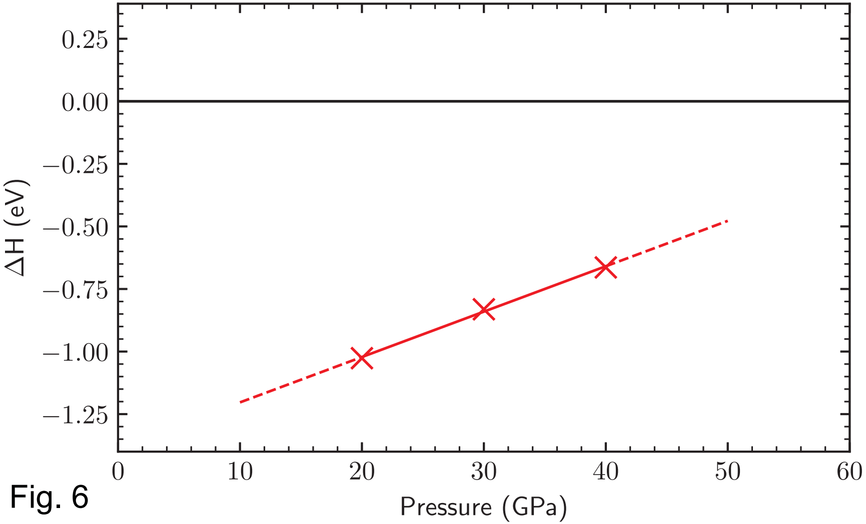

Fig. 6